BRAIN MENINGES SURFACE RECONSTRUCTION: APPLICATION TO LONGITUDINAL STUDY OF NORMAL AGING

by
Peiyu Duan

A thesis submitted to Johns Hopkins University in conformity with the requirements for the degree of Master of Science in Engineering

Baltimore, Maryland
May, 2022

Abstract

The cranial meninges are membranes enveloping the brain. The space between two of these membranes contains cerebrospinal fluid. Changes in the meninges have been associated with many neurodegenerative diseases. It is of interest to study how the volumes of this space change with respect to normal aging. In this work, we propose to combine convolutional neural networks (CNNs) with nested topology-preserving geometric deformable models (NTGDMs) to reconstruct meningeal surfaces from magnetic resonance (MR) images. We first use CNNs to predict implicit representations of these surfaces then refine them with NTGDMs to achieve sub-voxel accuracy while maintaining spherical topology and the correct anatomical ordering. MR contrast harmonization is used to match the contrasts between training and testing images. We applied our algorithm to a subset of healthy subjects from the Baltimore Longitudinal Study of Aging for demonstration purposes and conducted longitudinal statistical analysis of the intracranial volume (ICV) and subarachnoid space (SAS) volume. We found a statistically significant decrease in the ICV and an increase in the SAS volume with respect to normal aging. Additionally, we conducted a preliminary study on 5 subjects, in which we assigned region labels to the meninges—using a fast marching algorithm from cortical labels—and calculated the thickness of the meningeal layers. In the future, we hope to apply the algorithms to larger datasets to further study the regional thickness changes in the meninges.

Thesis Readers

Jerry L. Prince (Primary Advisor)
Professor
Department of Electrical and Computer Engineering
Department of Biomedical Engineering
Johns Hopkins University

Junghoon Lee
Associate Professor
Department of Radiation Oncology
Johns Hopkins University

Aaron Carass
Associate Research Scientist
Department of Electrical and Computer Engineering
Johns Hopkins University

Acknowledgements

I would like to thank everyone who devoted time and effort into helping me write and edit this thesis. I would like to express my deepest appreciation to my research advisor, Dr. Jerry Prince, who provided a tremendous amount of support and guidance over the past two years. He is always able to find time to talk to me and give me new ideas to help solve problems during the research progress. He showed me what finding passion in life means and has encouraged me to find my own passion in research.

I am also grateful to all the members in the Image Analysis and Communications Lab (IACL) who have always provided feedback in a timely manner and never resisted to help me during my time there. Speical thanks to Dr. Han and Dr. Xue in the IACL group who I got the chance to spend most time with. They were always generous with their time and were always willing to teach me stuff that I was not able to comprehend right away. Dr. Xue even took his personal time off to discuss papers that I could not understand and provided me new ideas for my future research. Without the help of them, I would not be able to understand the importance of details and present by myself at a conference.

Last but not least, I would like to thank my parents for their words of encouragements and support during the difficult times. Because of COVID, I have not had a chance to visit them for a very long time, but they continued to show their love and support through various ways possible. I will be forever grateful for their words of affirmation and always cheer for me at the lows. I became a better version of myself because of them, and their love encouraged me to pursue my passion in life.

Contents

List of Tables

List of Figures

Chapter 1

Introduction

1.1 Motivation

Neurodegenerative disorders have affected an increasing number of people worldwide due to population aging [1]. In the US alone, neurodegenerative diseases have affected more than 7 million people in total [1]. The top three neurodegenerative diseases are Alzheimer's disease (AD), Parkinson's disease (PD), and amyotrophic lateral sclerosis (ALS). Breakdown of the blood-brain barrier (BBB), a major neurodegenerative disease pathology, has been observed in not only rodents but also in humans [1]. In recent years, neuroimaging studies have found that individuals with mild cognitive impairment or in the early stage of AD also show signs of BBB breakdown [2, 3]. Similarly, blood central nervous system barrier (BCNSB) disruption has also been detected in ALS patients. These findings suggest that blood barrier disruptions in the brain can potentially contribute to neurodegenerative diseases. The brain meninges is located between the inner skull and the outer layer of the BBB [4]; thus, it is important to study the meninges to better understand aging. Considering the increased impact of brain aging related problems, it is crucial to study the size and volume changes of normal-aging trajectories of key structures related to the brain and the brain meninges and compare them with those in disease conditions.

The brain meninges is composed of three distinctive layers: dura mater, arachnoid mater, and pia mater. Figure 1-1 shows the anatomical structure of the brain meninges. The

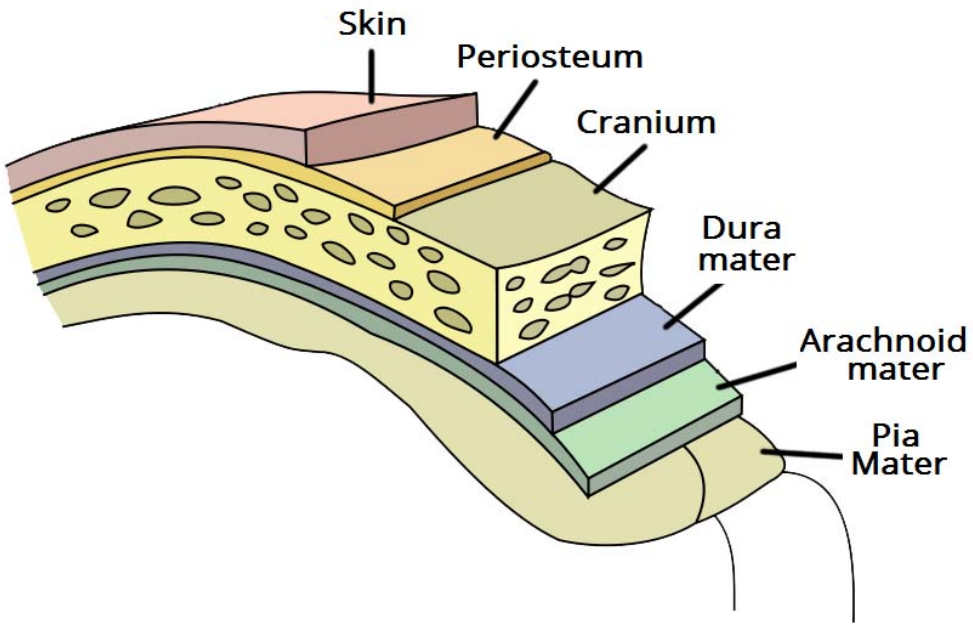

Figure 1-1. Brain meninges structure. [8]

three layers of meninges help maintain the mechanics, homeostasis, and immune response of the central nervous system [5]. These distinctive layers help to define clinically interesting volumetric measurements for brain studies. The subarachnoid space (SAS) is defined as the space between the arachnoid mater and pia mater. The volume changes in SAS imply the change in cerebrospinal fluid (CSF) distribution, which sheds light on brain atrophy and other neurodegenerative disease studies, such as AD and PD. [6, 7]. Besides the importance of SAS volumes, the total intracranial volume (ICV) is also an important normalization measure to correct for the head size [9, 10]. ICV is defined as the volume enclosed by the dura mater; more specifically, it is the volume enclosed by the epidural surface of the brain. ICV is also a well-known source for comparing between-subject variability in both total and regional brain volumes [9]. However, despite the significance of SAS and ICV, there have been very few studies on finding the changes in them during brain-aging.

One way to study the brain meningeal structures and their volumetric changes is to perform medical image segmentation [11]. Image segmentation delineates anatomical structures via

manual, semi-automatic algorithm, and automatic algorithms. Manual delineations are often done by experts to accurately identify the object and its boundaries. The delineations are often done on 2D slices of 3D images. There is also existing software that can help display the 3D images in different orientations to label regions of interest. For example, the software ITK-SNAP [12] allows the users to choose different colors for the segmentation labels and then manually segment the images. Manual segmentation is a time-consuming task and relies heavily on experts and has low intra-individual reliability. Semi-automatic segmentation helps reduce the segmentation time compared with manual delineations; however, inputs from experts are still required and can be time-consuming if the study requires a large amount of data. When analyzing large datasets to predict trends with clinical impacts, we must use automatic segmentation algorithms to speed up the process.

The algorithm presented in this thesis use multiple types of magnetic resonance (MR) images as input. Although MRI is one of the most widely used imaging modalities to analyze the brain and its structures due to its high soft-tissue contrast, the ultra-thinness of meningeal layers makes it difficult to directly segment them from conventional MR images. Figure 1-2 shows an example of paired T1w and T2w MR images. The pia and arachnoid surfaces can be seen on T2w MRI since the CSF contrast is bright on T2w images. The dural sinuses can also be seen in post-contrast T1w images. It is difficult to see bones in MRI, thus, when considering the training for the algorithm, we use a dataset containing CT data to find the epidural boundary.

Voxel-based segmentation algorithms are not good enough for meninges segmentation because meninges require sub-voxel resolution. In order to directly segment each meningeal layer and to accurately measure the volumes of SAS and ICV with sub-voxel resolution, we used deformable models to reconstruct the boundaries of individual meningeal surfaces. Our reconstruction pipeline is based upon a previous algorithm [13], which used a nested topology-preserving geometric deformable model (NTGDM) [14]. However, that previous work focused only on reconstructing the pia and arachnoid surfaces. Our work improved on

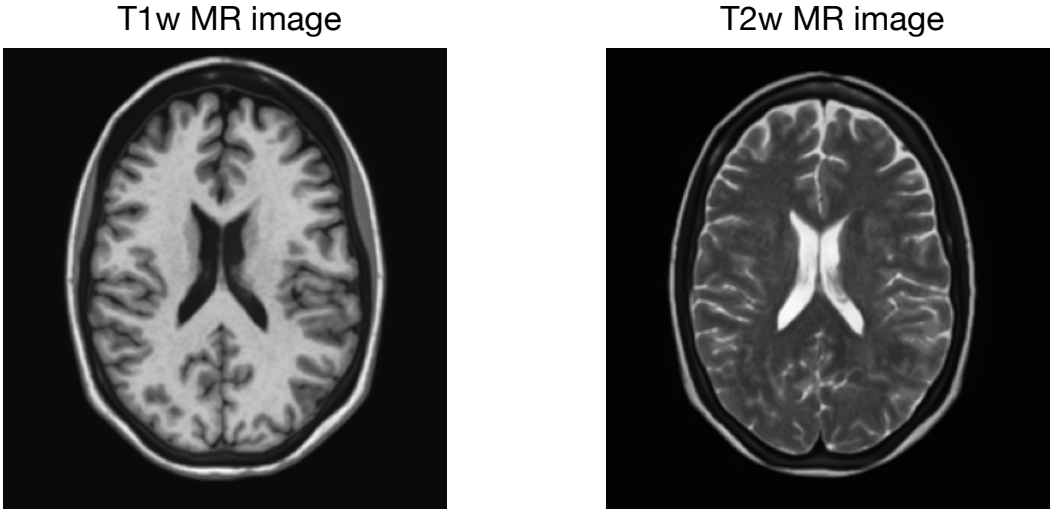

Figure 1-2. Example paired T1w and T2w MR Image.

the previous work by combining 2D U-Net convolutional neural network with NTGDM. We also extend the previous work to reconstruct and further analyze the pia, arachnoid, and dura boundaries. We applied our algorithm to 56 healthy, older participants with 243 MR imaging sessions from the Baltimore Longitudinal Study of Aging (BLSA) [15]. We were able to find the longitudinal changes in SAS and ICV and compare the differences between age, sex, and follow-up intervals.

1.2 Thesis Contributions

There are three main aims of this thesis.

(1) Develop an automatic algorithm to directly segment brain meninges from T1-w and T2-w Magnetic Resonance (MR) Images

Based on the previous work of NTGDM from Glaister et al.[13] in 2018, we were able to adapt a deep learning approach to directly segment each brain meningeal layer. We were able to achieve sub-voxel accuracies when estimating the boundaries of each meninges, which was

crucial due to the thinness of each meningeal layer. After segmenting the dura, arachnoid, and pia layers individually, we were able to separately reconstruct the three meningeal surfaces.

(2) Analyze the longitudinal changes of SAS and ICV

Pilot studies were carried out by applying the algorithm in the first aim to 56 subjects from the BLSA [15]. We were able to calculate volumes enclosed by the epidural surface as ICV measurements and volumes between the arachnoid surface and pia surface as SAS volume measurements. The volumes were statistically analyzed to observe the volume changes during normal aging.

(3) Preliminary dura thickness calculation with region labeling

A preliminary study was conducted on 5 BLSA subjects with 18 imaging sessions to investigate whether dura thickness changes regionally during normal aging. To aid future analysis on regional thickness changes, we used fast marching [16] to march the SLANT labels of the cortical brain surfaces to the meningeal surfaces. In the future, we can divide the meningeal surface labels into different cortical regions to analyze meningeal layer thickness changes at a regional level.

1.3 Thesis organization

The thesis is organized as follows. In Chapter 2, we start by providing the background information of this thesis. We first introduce the brain meningeal anatomical structures. We provide definitions of the key structures, which are the focus of this thesis. We also address the importance of such anatomical structures and their use in aging studies. In Section 2.2, we review current methods and studies, which are divided into two subsections. Subsection 2.2.1 reviews the literature on brain meninges segmentation methods and states the current problems in direct meninges segmentation methods. We also note the lack of existing literature on meninges longitudinal analysis. In subsection 2.2.2, we review four different types of deep learning based surface reconstruction methods. At the end of chapter 2, we address the current challenges in direct meninges segmentation and state the innovation

and motivation for our studies.

Chapter 3 focuses on the methods that were used in this thesis. We first introduce the dataset used for this study. Next, we describe the image processing steps for both training data and testing data in detail before our 2D U-Net network training. Several existing algorithms were used to improve the image quality of our data. In Section 3.3, we first discuss our general network structure with an illustration of the U-Net architecture. The section then divides into three subsections to talk about the U-Net training and testing of each meningeal surface. Two separate 2D U-Nets are trained to each predict a soft segmentation of one meningeal surface. Arachnoid segmentation training is introduced first and then followed by epidural surface segmentation training. U-Net testing is combined into one subsection after the U-Net training of the arachnoid and epidural surface soft segmentation. In Section 3.4, the method for arachnoid and dura surface reconstruction is provided. Then, methods for region mapping of meninges and preliminary study of dura thickness calculation are introduced. At the end of the chapter, the main method for our statistical analysis, the linear mixed effect (LME) model, is introduced. We also have a section on how to use the LME model to conduct statistical analysis.

In Chapter 4, we discuss the results of our studies. The surface reconstruction results are illustrated in two different ways. One way is to align the surface reconstruction results into the voxel grids of BLSA subject's MR images. Another way is directly show the 3D surface reconstruction result of meningeal surfaces. Then, an algorithm validation is done to verify our LME analysis result. At the end of the chapter, we describe the preliminary results of region mapping with dura thickness calculation for 5 subjects.

In the final chapter, we summarize the discoveries from our studies and conclude the thesis. We also discuss our findings and provide directions for future studies.

Chapter 2

Background

2.1 Key Structures of the Meninges

The cranial meninges are thin membranes enclosing the brain. The average thickness for dura mater is 0.36 mm [17] and the average thickness for arachnoid and pia mater is about 0.015–0.04 mm [18]. The dura mater is directly adherent to the inner surface of the skull, and there is typically no space between the dura and arachnoid. The inner most layer of meninges is the pia mater.

The SAS is tightly connected by trabeculae connective tissues, which form a spider web appearance [19]. The SAS mainly contains the cerebrospinal fluid (CSF) in the triangular spaces of the meninges. CSF serves as a nutrient delivery and waste removal system for the brain [20], and it is manufactured continuously in brain ventricles. Because of the importance of CSF, we are interested in analyzing the size change of the SAS to study how the CSF is distributed during normal aging, and it can also provide an alternative way to study brain atrophy. Another key indicator of brain changes is the ICV. The ICV includes the white matter, gray matter, veins, and meninges. We are also interested in studying the size of the ICV during normal aging since ICV has often been used to adjust for the head size when studying the size of brain structures [9, 10]. Additionally, some of the differences in brain volumes between biological sexes can also be accounted for and adjusted with ICV.

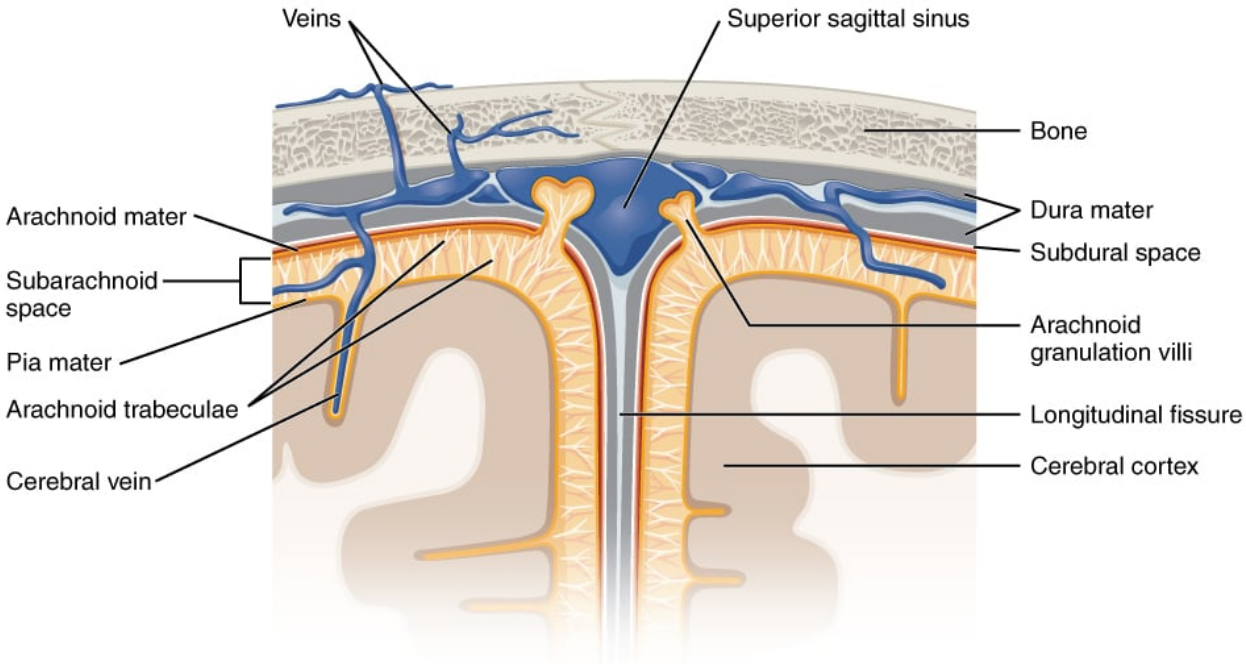

Figure 2-1. Anatomical structure of brain meninges with CSF. The layers of the meninges of the superior sagittal sinus are shown, with the dura mater adjacent to the inner surface of the cranium, the pia mater adjacent to the surface of the brain, and the arachnoid mater and the subarachnoid space between them. An arachnoid granulation villi is shown on the right side of the image emerging into the dural sinus. The arachnoid granulation villi filter CSF back into the blood for drainage. [21]

2.2 Existing Methods and Studies in Literature

2.2.1 Meninges Segmentation and Longitudinal Literature

There are very few existing methods for directly segmenting meningeal layers. In 2014, one method was published in Neuroimage to automatically segment the cortical surface of the brain, which is equivalent to segmenting the pia surface. [22]. However, the computational framework requires a 7T MRI scan with specialized magnetization-prepared rapid gradient-echo (MP2RAGE) sequence, which is not routinely collected [22]. Another method [23] uses multimodal images such as fluid-attenuated inversion recovery (FLAIR) and multi-echo MPRAGE (MEMPRAGE), to segment brain tissues. However, it only mentions the segmentation of dura excluding other parts of the meninges. Additionally, it focuses on separating gray matter from the dura, while the arachnoid layer is in between the gray matter

and the dura mater.

There have also been limited aging studies on longitudinal ICV change. In 2003, Liu et al. did a longitudinal and a cross-sectional analysis of ICV change [24]. They evaluated volume changes in three different age epochs: ones that are younger than 35; ones that are between 35 and 54; and ones that are older than 54 years old. However, their longitudinal analysis only had 5 subjects showing significant longitudinal changes over the 90 healthy subjects they performed analysis on. Additionally, the changes they found were only a small increase (about 4.6 ml) in the youngest group. However, their cross-sectional study revealed a significant association between age and reduction in all brain volumes except the hippocampal volume. In 2013, another group of researchers from the UK found that the inner table of the skull thickens for older people, reducing ICV by an average of 101 mL for males and 114 mL for females. Their ICV measurements were done using semi-automatic delineation methods and consulted experts to estimate the original ICV excluding the effects of skull thickening [25]. In 2020, Mount Sinai and Dutch researchers assessed aging in young and middle adulthood also applying a semi-automatic in-house built algorithm on T1w MR brain scans to measure ICV change [26]. They scanned individuals between the ages of 16 and 55 up to three consecutive times with an average of 3.3 yrs between consecutive scans. Their cross-sectional analysis reported a statistically significant increase in the ICV in adulthood until the fourth decade of life and a decrease in the ICV afterward. Even though this study reported changes in ICV, it did not focus on adults older than 55 and their ICV changes.

2.2.2 Surface Reconstruction Literature

Over the past few years, deep learning based approaches have mostly been focused on cortical surface reconstruction instead of individual meningeal layers. The related works can be divided into four main categories and described in the following.

(1) **Voxel-based surface reconstruction**: SegRecon [27] uses a 3D CNN model that reconstructs and segments surfaces directly from 3D T1-MRI volumes. The network learns

a signed distance map prediction from the input MRI volume. To reconstruct the cortical surface, SegRecon applies Gaussian smoothing to the predicted map, then uses marching cubes and topology correction to obtain the surface. FastSurfer [28] is another voxel-based surface reconstruction deep learning pipeline. The pipeline replicates FreeSurfer's anatomical segmentation including the surface reconstruction but speeds up the segmentation processing time to less than 1 min on the GPU. The network is composed of competitive dense blocks for the encoder and decoder part and takes 2D slices of MR images from coronal, axial, and sagittal directions. The surfaces are reconstructed with the marching cubes algorithm. Then, a spectral mapping to the sphere is carried out. The limitation with voxel-wise surface reconstruction is that it heavily relies upon the resolution of the images, which can lead to calculation errors if the segmentation object requires sub-voxel accuracy.

(2) **Mesh-based surface reconstruction**: Voxel2Mesh [29] utilizes a 3D voxel encoder, a voxel decoder, and a mesh decoder to obtain a mesh representation of an input MR Images. The network takes 3D volumetric images and a spherical mesh as input, and the mesh decoder learns to deform the mesh iteratively according to the learned neighborhood sampling of the output of the voxel decoder to form an accurate mesh representation of the image object. The model also uses an adaptive mesh unpooling strategy to represent high-curvature regions with more vertices than other regions, to increase memory efficiency.

Another deep-learning based method, PialNN [30] reconstructs the pial surface with the input of the white matter surface and the corresponding MR image. PialNN applied three deformation blocks to the white matter surface and Laplacian smoothing to obtain the final pial surface mesh. Within each deformation block, 3D CNN incorporates the features from the vertices in the mesh and features from the MR images.

(3) **Deep implicit representations** Another popular method for surface reconstruction uses deep implicit representations. Generally, a function, such as a signed distance function, can be learned that maps 3D coordinates to a continuous implicit shape representation [31]. A popular method using deep implicit representation to reconstruct the cortical surface from

MRI is DeepCSR [32]. The network takes MRI as input and outputs a mesh representation of the outer and inner cortical surfaces. After performing registration into an MNI space, it constructs a cartesian point grid by dividing into evenly spaced points [32]. Similar to our method, it also requires a topology correction step using topology preserving marching cubes.

(4) **Fast explicit representation surface reconstruction**: TopoFit [33] trained joint deep networks consisting of U-Net and a graph-convolutional networks to reconstruct the white matter mesh with a template mesh and MR image as input. The U-Net extracts the spatial features from the MR image while the graph-convolutional network learns the warp transformation by sampling these extracted features to obtain the target white matter mesh. Vox2Cortex [31] is a geometric deep learning based method for fast reconstruction of the cortical surface. The pipeline takes in a 3D brain MRI and a Laplacian smoothed mesh template as input to the network. The architecture of the network combines a convolutional neural network and a graph neural network (GNN). However, fast explicit mesh representation methods could potentially have the problem of self-intersection, which can lead to inaccurate estimation of volumes.

2.3 Summary

Despite the importance of the SAS and ICV, very limited study has been done to observe their structural and volume changes during aging. Indeed, there has been no longitudinal study on SAS changes during aging. Additionally, the current deep learning based methods only segment part of the meninges and have been focused primarily on reconstructing the cortical surface.

Chapter 3

Methods

3.1 Datasets

We selected 56 subjects from the BLSA, comprising 28 age-matched cognitively normal males and females, with 243 visits in total, see Table 3-I for complete demographic details. We use the age at the first visit as the baseline age and define the follow-up interval as the age difference in years between a visit and the baseline age. The baseline ages for all subjects range from 70 to 88 years with an average of 78.24 years for the females and 78.15 years for the males. The follow-up intervals range from 0.8–10.7 years (average 2.97 years) for all subjects. For our processing, we used paired T1w and T2w MR images.

Table 3-I. Baltimore Longitudinal Study of Aging Dataset.

	Overall	**Male**	**Female**
Number of Subjects	56	28	28
Number of Visits	243	123	120
Baseline Age (yrs)			
Mean (SD)	78.19 (5.4)	78.15 (5.37)	78.24 (5.6)
Range	70-88	70-88	70-88
Follow-up (yrs)			
Mean (SD)	2.97 (2.54)	3.14 (2.7)	2.78 (2.31)
Range	0.8-10.7	0.8-10.7	0.8-9.3

3.2 Image Preprocessing

The BLSA images were acquired on Philips Achieva 3.0 T MR scanner. The T1w and T2w images were inhomogeneity-corrected using N4 [34]. The mean white matter intensity of each contrast was separately normalized to 1,000 [35]. The T2w images were super-resolved in the through-plane direction using SMORE [36, 37]. The T1w, T2w, and CT images were coregistered into a $0.8 \times 0.8 \times 0.8$ mm^3 MNI space [38]. The corresponding manual delineations from the CT images were then mapped into the same space. The training data [39, 40], contains 6 subjects for the arachnoid surface training and 6 subjects for the dura surfaces training. However, there is a contrast variation problem between the paired T1w and T2w training data and the BLSA testing data, which could degrade the performance of the trained model on the testing data. To minimize this problem, we ran a harmonization algorithm, CALAMITI [41, 42], to harmonize the training data to the BLSA contrasts. Figure 3-1 shows the contrast adjustment comparisons before and after CALAMITI is performed. Figs. 3-1 (A) and (B) show paired T1W and T2w training data before harmonization, respectively; Figs. 3-1 (C) and (D) are the paired T1w and T2w BLSA MR harmonization target image, respectively. We can see that Figs. 3-1 (A) and (B) have different contrast than Figs. 3-1 (C) and (D) due to the differences in the used MR sequences. We can use CALAMITI to convert the contrast of Figs. 3-1 (A) and (B) to the targeted images (C) and (D) while maintaining the same anatomy. Figs 3-1 (E) and (F) show the result after CALAMITI is performed. We can see that Figs. 3-1 (E) and (F) have similar contrast with Figs. 3-1 (C) and (D) but maintains the same anatomy as the original T1w and T2w images. We used SLANT-CRUISE [43, 44] to reconstruct the pia surface.

3.3 2D U-Net Convolutional Neural Networks

We trained two 2D U-Net CNNs [45] independently, one for the dura and one for the arachnoid. Each predicts a segmentation, which can be represented mathematically as an occupancy

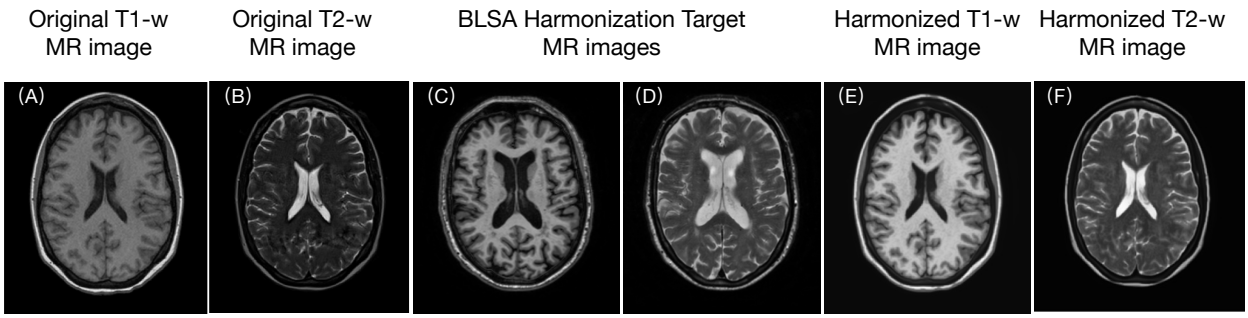

Figure 3-1. CALAMITI Contrast Adjustments.

function, $o : \mathbb{R}^3 \rightarrow [0, 1]$.

An occupancy function can be predicted by our convolutional neural networks in which every location p of the 3D MR image ($p \in \mathbb{Z}^3$) is assigned an occupancy probability between 0 and 1 [46]. To predict a 3D mask with a 2D network, we first extracted all slices along each of the three cardinal orientations and then fed these images into the network. The three outputs of the network are then combined by taking the median value of each voxel for the three orthogonal slices that include that voxel. The final 3D mask is then obtained by thresholding this "median" image at 0.5. For this project, we concatenated paired T1w and T2w slices (again, extracted from all three orientations) as input to the U-Net network. The network architecture is shown in Fig 3-2. Our modified U-Net contains 64 channels after the first convolution block and 5 downsampling steps. 2D slices of paired T1w and T2w images, which were extracted from all three of axial, coronal, and sagittal orientations, were used as a double-channel input to the networks. Both networks were optimized using the Adam optimizer [47] with a learning rate of 2×10^{-4} for 100 epochs and a mini-batch size of 8.

3.3.1 2D U-Net Training for Arachnoid Segmentation

The training data for arachnoid segmentation includes the paired T1w and T2w images from Roy et al. [40]. To obtain the training arachnoid masks, a skull-striping algorithm, MONSTR algorithm [48], was applied to these images. We chose 6 subjects from this dataset as the

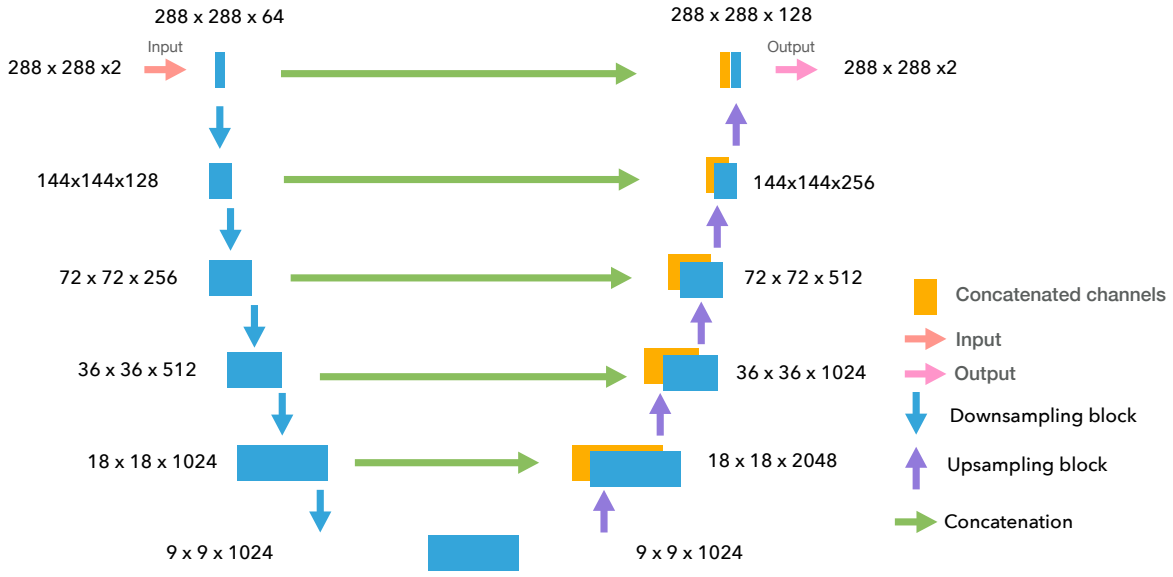

Figure 3-2. The 2D U-Net CNN structure. In the downsampling path, we decrease the image height and width by a factor of 2, and increase the image channels by a factor of 2 each time. The maximum number of channels in the downsampling path is capped at 1,024. In the upsampling path, we increase the image height and width by a factor of 2 with upsampling and decrease the image channels by a factor of 2 each time. The result of each downsampling block is concatenated with the upsampling block result shown as green arrows. The output of the image contains two channels, which are the predicted occupancy maps of the dura and arachnoid surfaces. The occupancy maps are further binarized to form hard segmentation masks.

training data for the arachnoid segmentation 2D U-Net. To train this network, a binary cross entropy loss function:

$$BCE = -\frac{1}{N}\sum_{i}^{N}(y_i \log(\hat{y}_i) + (1-y)\log(1-\hat{y}_i)) \tag{3.1}$$

was applied, with the optimization approach specified in Sec. 3.3. In binary cross entropy loss function, N is the total number of voxels in the training batch, $\hat{y}_i$ is the predicted probability of whether the voxel i is inside the arachnoid surface, and y_i is segmented result from the training data of voxel i.

3.3.2 2D U-Net Training for Dura Segmentation

To train the U-Net for dura segmentation, we manually delineated the dura for 20 BLSA subjects to construct a training dataset. To make the prediction more accurate, CT delin-

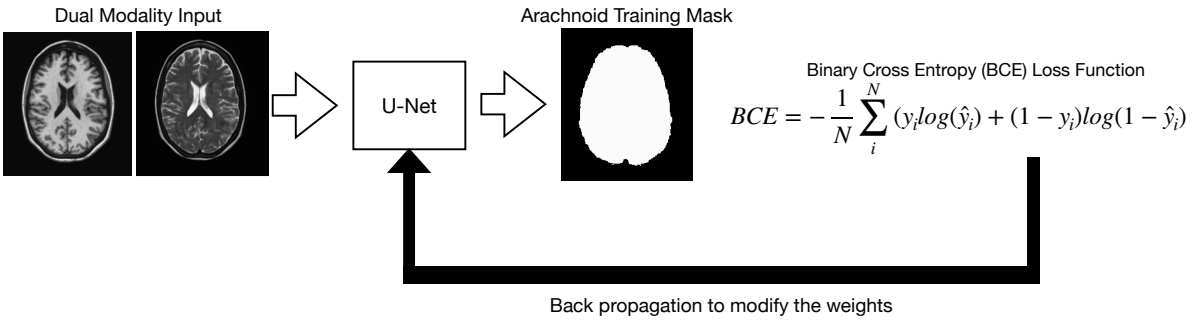

Figure 3-3. Slices are extracted from images along axial, sagittal, and coronal planes, and T1w and T2w slices were concatenated as 2 channels to be the input of U-Net. In this figure, only paired axial plane slices of T1w and T2w images are shown. During the training, a binary cross entropy loss function was applied to compare the U-Net prediction of the mask and the arachnoid training mask to backpropagate the gradient for the Adam Optimizer to update the weights in the U-Net.

eations from Singh et al. [39] were used to better estimate the epidural surface, as the CT is more suitable for visualizing the skull. CT images are used to help define the boundaries for the epidural surface of the dura mater. The U-net also used paired T1 and T2w images as input. The network output both a synthetic CT and a soft segmentation map of the epidural surface. Mean squared error loss:

$$MSE = -\frac{1}{N}\sum_{i}^{N}(\hat{y}_i - y_i)^2 \tag{3.2}$$

was used for the synthesized CT image and binary cross entropy loss, Equation 3.1, was used for epidural soft segmentation prediction, where the prediction result for each voxel could be interpreted as a probability. The optimization method is the same as mentioned in Sec. 3.3

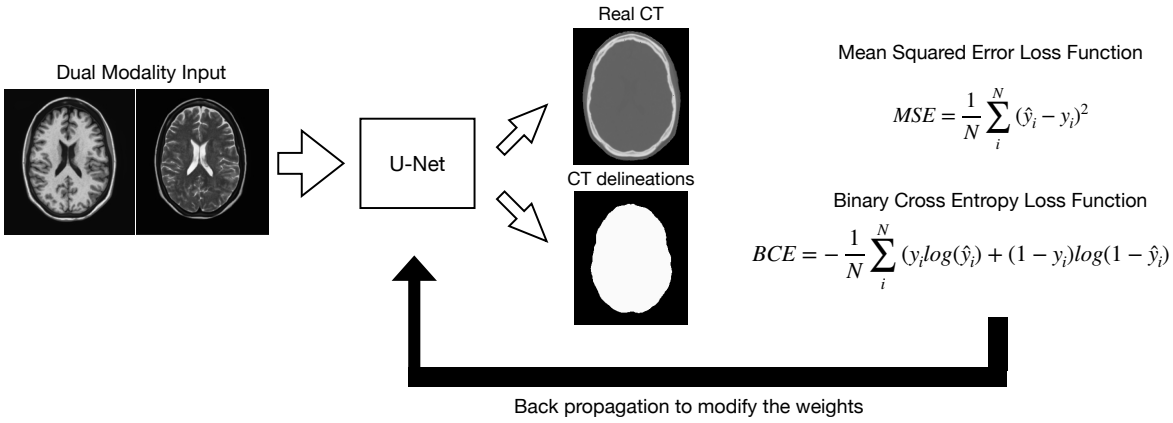

Figure 3-4. T1w and T2w slices were concatenated as two channels to be the input of the U-Net in the same manner as Fig. 3-3. Different from the arachnoid segmentation U-Net, the dura segmentation U-Net provides an output that has two channels: one channel is a synthesized CT image while the other channel is the dura segmentation prediction. Here, the binarized dura hard segmentation is shown. Binary cross entropy loss function was applied to soft segmentation results to compare the U-Net prediction of the dura mask and the training mask which is manually delineated from a reference of CT images. A mean squared error loss function is applied to compare the output of synthesized CT from MR image and the real CT. The gradients of the errors are then back-propagated to update the weights in U-Net.

3.3.3 Apply 2D U-Nets

During testing, the network was applied to all paired T1w and T2w BLSA images. The occupancy map is formed by taking the median occupancy value of each voxel from three orientations. The hard segmentation masks obtained from binarizing two 2D U-Net soft segmentations are shown in Fig. 3-5. The 2D U-Net for epidural soft segmentation outputs both a synthetic CT image and also an epidural soft segmentation. Since we used real CT images for training, outputting a synthetic CT from a double modality input MRI could be useful for comparing epidural mask results as well as for other downstream tasks. The arachnoid 2D U-Net network outputs only one channel, which is the arachnoid soft segmentation. Although we harmonized the training data to the BLSA contrasts, the

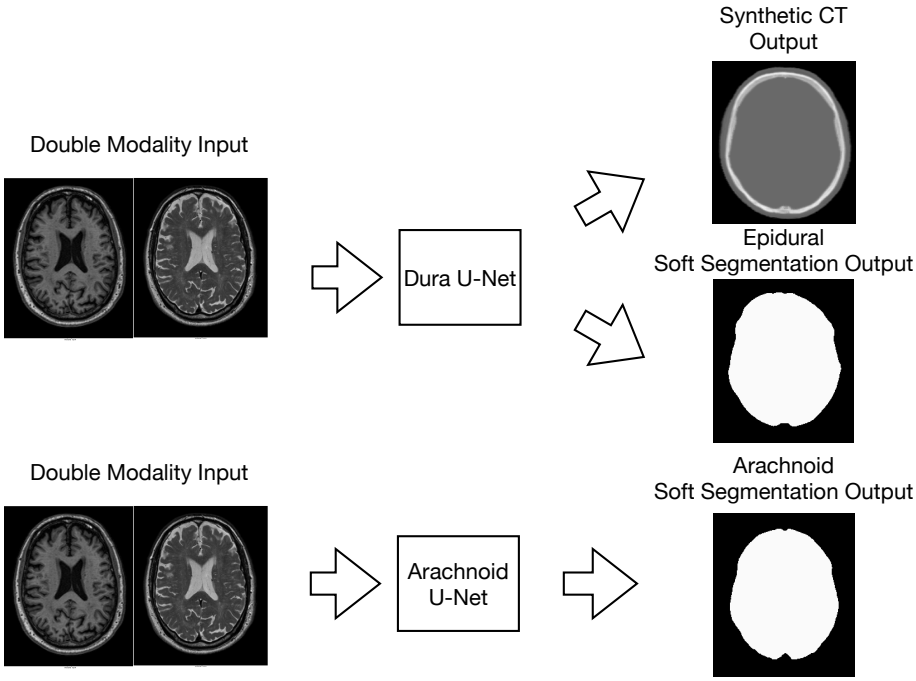

Figure 3-5. Two previously trained 2D U-Nets were applied to the harmonized dataset. As previously mentioned in Sec. 3.3, paired T1w and T2w slices were extracted in three planes and concatenated as two-channel input to the trained U-Net CNN. The dura segmentation 2D U-Net output the synthetic CT image and the epidural soft segmentation while the arachnoid 2D U-Net outputs the arachnoid soft segmentation. Here we show the hard segmentations obtained from binarizing the soft segmentations for visualization purposes.

predictions were still not robust due to the discrepancy between the two training sites. Therefore, we manually corrected three predicted occupancy masks for each of our two networks to fine-tune them for another 10 epochs. There was no further manual intervention after network fine-tuning.

3.4 Arachnoid and Dura Surface Reconstruction

After we obtained the soft segmentation of the arachnoid and epidura surfaces, we applied two NTGDMs [13, 14] to reconstruct the arachnoid and dura surfaces. In NTGDM, the

evolution process of the level set function Φ is defined as

$$\Phi_t(\mathbf{x},t) = F_{\text{prop}}\,(\mathbf{x})\|\nabla\Phi(\mathbf{x},t)\| + F_{curv}(\mathbf{x})\|\nabla\Phi(\mathbf{x},t)\| + \vec{F}_{adv}\cdot\nabla\Phi(\mathbf{x},t), \tag{3.3}$$

where F_{prop}, F_{curv}, and F_{adv} are the propagation, curvature, and advection speed function, respectively. In our experiments, we did not use the advection speed function, so only propagation and curvature terms were used. To ensure a correct nested topology, an additional constraint is added to make sure $\Phi_{dura}(x)$ cannot be greater than $\Phi_{arachnoid}(x)$. In other words, the reconstructed arachnoid surface is guaranteed to be inside the epidural surface.

Unlike [13] which used a deformable registration from an atlas to achieve the region force mask and computed the initial level set function $\Phi(\mathbf{x},0)$ using the signed distance to the convex hull of the inner subarachnoid surface, we rescaled the predicted occupancy map values to the range $[-1,1]$ as the initial region forces to be used in NTGDMs. A signed distance function represents the distance between a surface and all image voxels; with interior voxels having negative distances and exterior voxels having positive distances. We used the largest connected component of the thresholded occupancy map (greater than 0.5) and a topology-correction algorithm [49] to generate a signed distance function with a spherical topology (a single closed surface without holes or handles) as the *initial* levelset of each NTGDM. The *inner* levelsets for NTGDMs of the arachnoid and dura were set as the pia and arachnoid surfaces, respectively, to guarantee the anatomical ordering of these surfaces. The weights for the curvature and region forces were set to 0.2 and 2, respectively. Finally, we calculated the ICV as the volume enclosed by the dura surface and the SAS volume as the volume between the arachnoid and pia surfaces using the triangular meshes that were generated from our NTGDMs.

3.5 Region Mapping and Thickness Calculation

To calculate the thickness of dura, we calculated the signed distance of the points on the dura to the surfaces of arachnoid reconstructed from Section 3.4. To decrease the number of points involved in the calculation for faster algorithm execution, we subsampled the dura surfaces by their vertices and rounded these coordinates to the nearest integers to map these coordinates to the image space. For the thickness of the arachnoid, we calculated the distances between the arachnoid surface and pia surface with the same methodology.

To analyze the meningeal thickness by cortical region, we need to label the vertices of the meningeal surface with the nearest cortical membership. Since the SLANT algorithm only assigns brain region memberships to the voxels that are inside the pia surface, we need to extend these memberships to the voxels outside the pia surface in order to determine the closest memberships of the points on the meningeal surfaces. We first used the fast marching algorithm [16] to extrapolate the cortical region labels to every voxel of the image. The fast marching technique for extending the label definitions is a region-growing method based on the level-set technique. The algorithm grows the region by extending the contours along their normal direction with the speed of F, T is the time of arrival function which states the time it takes for the level-set function to extend to that voxel. Therefore, the relationship could be described by Equation 3.4:

$$F|\nabla T| = 1 \tag{3.4}$$

which states that the gradient of the time-arrival function is the inverse of the region-growing speed F. In this scenario, the zero level sets are initialized by the boundaries of the regions of SLANT labels. All the unlabeled voxels that are characterized as inside the first evolving level sets are assigned the same labels as the initialized region.

To interpolate the memberships of points on the meningeal surfaces, we assigned the cortical region labels of the vertices of the meningeal surface to be the labels of the closest cortical voxel.

3.6 Linear Mixed Effects Models

Linear models are one of the most commonly used statistical models to analyze and examine correlations, interactions, and treatment effects [50]. A mixed-effects model has both fixed effects and random effects. Linear mixed effects models (LME) are extensions of the simple linear model. The advantage of using LME models instead of a linear model is that it can handle unbalanced data and handle correlations within and across subjects. Although we need to remove missing values, it only has a small effect in the mixed-modeling framework since each observation only represents a small part of many responses within a subject [51]. Random effects depend on individual experimental units that are randomly chosen from a population [50]. The parameters of random effects are random variables themselves. The benefits of including random effects for participants solves the nonindependence problem if the response rate varies when computing multiple regressions in-between subjects. Fixed effects parameters are associated with an entire population. These effects are expected to operate in a predictable way and should persist across experiments, meaning that the parameter does not vary [51]. We can assume that there is some true regression line in the population characterized by the slope β, and we can estimate it, with $\hat{\beta}$. In contrast, since random effects variables are distributed randomly, we can assume that β is a normally distributed variable with mean μ and standard deviation σ. In equation forms, the random distribution assumed can be expressed as below:

$$\beta \sim \mathcal{N}(\mu, \sigma) \tag{3.5}$$

The generalized linear mixed effects model in matrix notation is shown as following:

$$y = X\beta + Zu + \epsilon \tag{3.6}$$

where dependent variable y is a $N \times 1$ column vector of outcome observations, with mean $E(y) = X\beta$; X is a $N \times p$ design matrix of the p predictor variables; β is a $p \times 1$ column

vector of fixed-effects regression coefficients; Z is the design matrix for fixed effects with $n \times q$ dimensions; u is the $q \times 1$ vector of random effects coefficients; ϵ is a $N \times 1$ column vector of residual errors [50]. In LME, it is typically assumed that:

$$u \sim \mathcal{N}(0, G); \epsilon \sim (0, R); \text{Cov}(u, \epsilon) = 0 \tag{3.7}$$

The random effects are assumed to be sampled from a multivariate Gaussian distribution. We are interested in whether β statistically significantly differs from zero using a t-test.

3.7 Statistical Analysis

For statistical analysis, we used two LME models in R version 4.0.3 with the `nlme` library [52] to study the relationship between age and sex with baseline and longitudinal change in ICVs and SAS volumes individually.

For ICV analysis, we used the following equations to fit the LME model:

$$\text{Fixed effects} = (1 + \text{sex} + \text{baseline age} + \text{follow-up time}) \tag{3.8}$$

$$\text{Random effects} = (1 + \text{follow-up time}|\text{ID}) \tag{3.9}$$

The ID in the equation is the assigned subject ID for each individual. For SAS analysis, the following equations were used to fit the model:

$$\text{Fixed effects} = (1 + \text{sex} + \text{baseline age} + \text{follow-up time}) \tag{3.10}$$

$$\text{Random effects} = (1 + \text{follow-up time}|\text{ID}) \tag{3.11}$$

The fixed effects for the ICVs were the intercept, follow-up interval, baseline age, and biological sex. The fixed effects for the SAS volumes were the intercept, follow-up interval,

baseline age, sex, and ICV at the baseline visit. The baseline ages were centered around the mean of all subjects, i.e., 78.95 years. For the biological sex, we used 0.5 to indicate males and -0.5 to indicate females after centering. The random effects were the intercept and follow-up interval for both models. We then tested whether the coefficients of the fixed effects were significantly different from 0 (p-value< 0.05).

Chapter 4

Results

4.1 Surface Reconstruction

The 3D meninges surfaces (pia, arachnoid, and epidural) of one patient reconstructed from the levelset functions, are shown in Fig. 4-1. These surfaces have a higher resolution than the voxel grid of the paired T1w and T2w images. To overlay the boundaries of the surface, the vertices of the surface meshes were interpolated to the voxel grid size in the T1 and T2 images and are shown in Fig. 4-2. In Fig. 4-2 we observed that even though the dura and arachnoid surfaces are close together, the dura surface is outside the arachnoid surface. This shows that the relative topology among these meningeal surfaces is preserved by the algorithm. These mesh surfaces were used to calculate the ICV and SAS volume for each visit.

4.2 LME Volume Analysis

We removed 31 failed cases during image registration and surface reconstruction, resulting in 212 visits in total for the following LME analyses. The volumes from all visits of all subjects are plotted in Fig. 4-3. The LME results are shown in Table 4-I. Both the sex and follow-up interval are significant predictors for the ICV. Males have statistically significant larger ICVs than females. Although the ICV is not significantly correlated with the baseline age cross-sectionally, it does significantly decrease over time. For the SAS volume, it is not

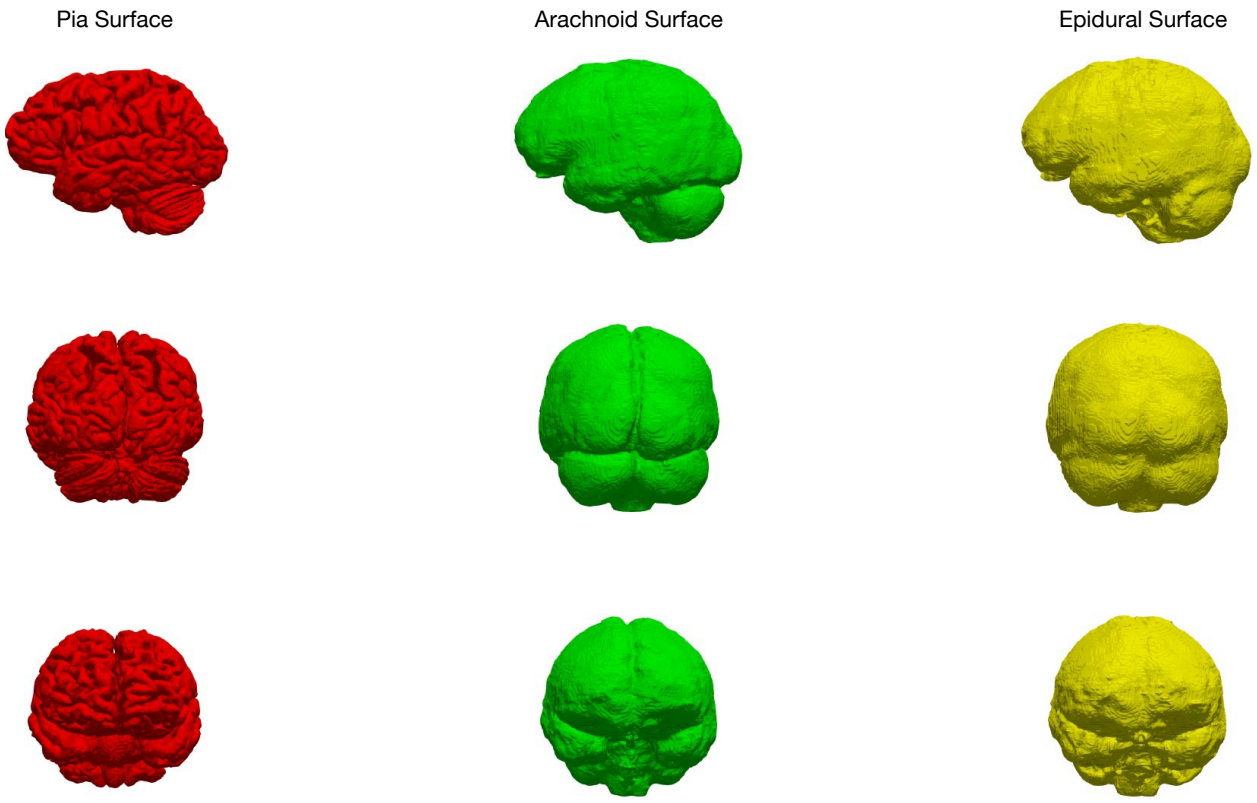

Figure 4-1. Example reconstructions of the dura (yellow), arachnoid (green), and pia (red) surfaces.

significantly correlated with the biological sex after adjusting for the ICV. Both the baseline age and follow-up interval are significant, which indicates that the SAS volume is larger at a higher baseline age and increases over time. We also plot the LME fits in Fig. 4-4.

Table 4-I. Fixed-effect coefficients (β), standard error (SE), and p-values (p) for the sex, baseline age, and follow-up interval. Statistically significant effects with p-values ≤ 0.05 are highlighted in bold.

	ICV			**SAS volume**		
	$\boldsymbol{\beta}$	**SE**	$\boldsymbol{p}$**-value**	$\boldsymbol{\beta}$	**SE**	$\boldsymbol{p}$**-value**
Sex	**144.60**	**28.91**	$\mathbf{6.87 \times 10^{-6}}$	9.54	11.51	0.41
Baseline age	-2.01	2.66	0.45	**1.87**	**0.87**	$\mathbf{3.66 \times 10^{-2}}$
Follow-up interval	**-1.38**	**0.23**	$\mathbf{1.35 \times 10^{-8}}$	**2.42**	**0.41**	$\mathbf{2.82 \times 10^{-8}}$

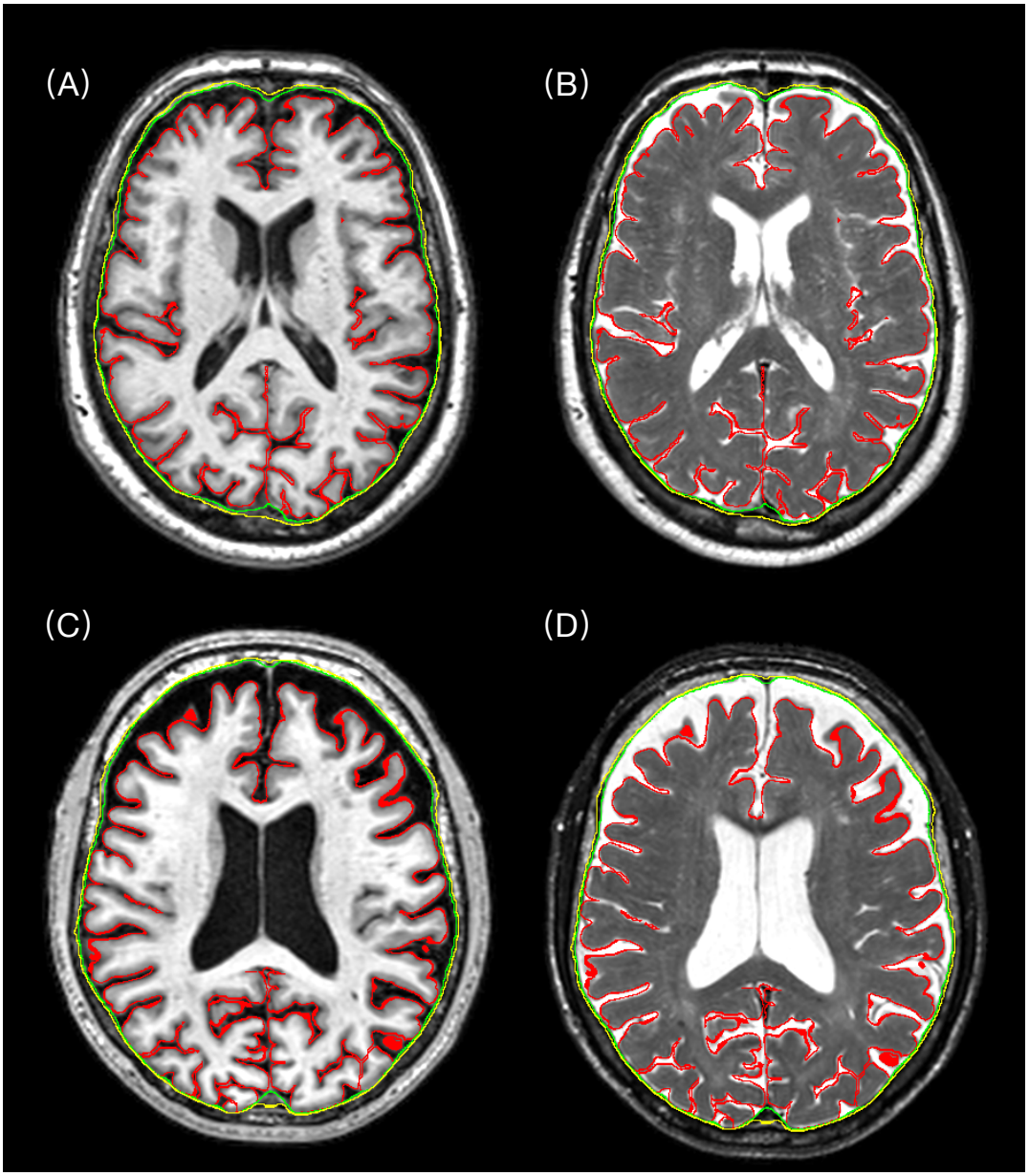

Figure 4-2. Example reconstructions of dura (yellow), arachnoid (green), and pia (red) surfaces. (A) and (B) are T1w and T2w images of a subject, respectively. (C) and (D) are T1w and T2w images of another subject, respectively. The surfaces are interpolated to the voxel grids of the T1w and T2w image slices.

4.3 Partial Volume Effects Evaluation on Algorithm

Our longitudinal results show that SAS volumes increase with aging, meaning that CSF volume is also increasing. However, our results suggest that ICV decreases with aging, which seems odd since it is often assumed that the skull maintains its size after early adulthood.

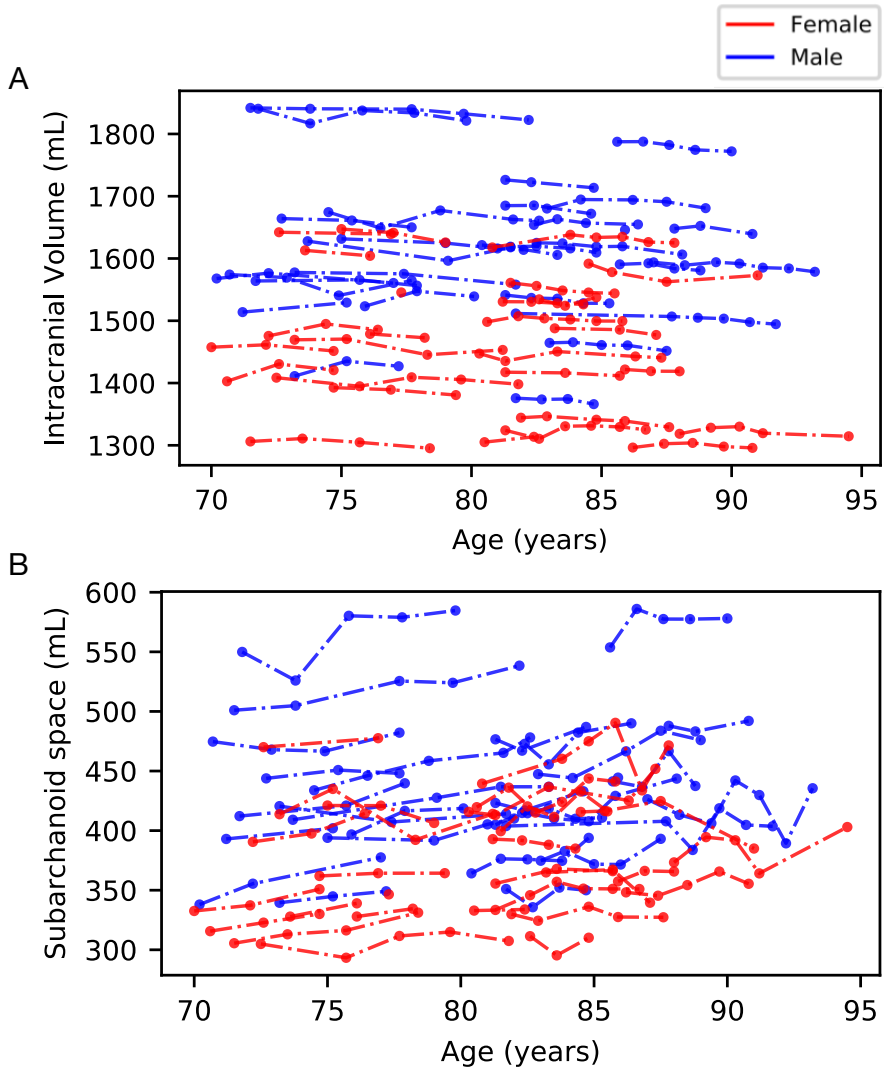

Figure 4-3. The trajectories of individual volumes of all subjects and visits. Each dot represents the volume measurement at a visit from an individual, with a patients sequence of visits connected by dashed and dotted line. Males and females are plotted in blue and red, respectively. (A) is ICVs, and (B) is SAS volumes.

Thus, we wanted to verify that this result is not the result of algorithm bias. Since CSF increases during aging, the partial volume effects could pose a challenge to the accuracy of

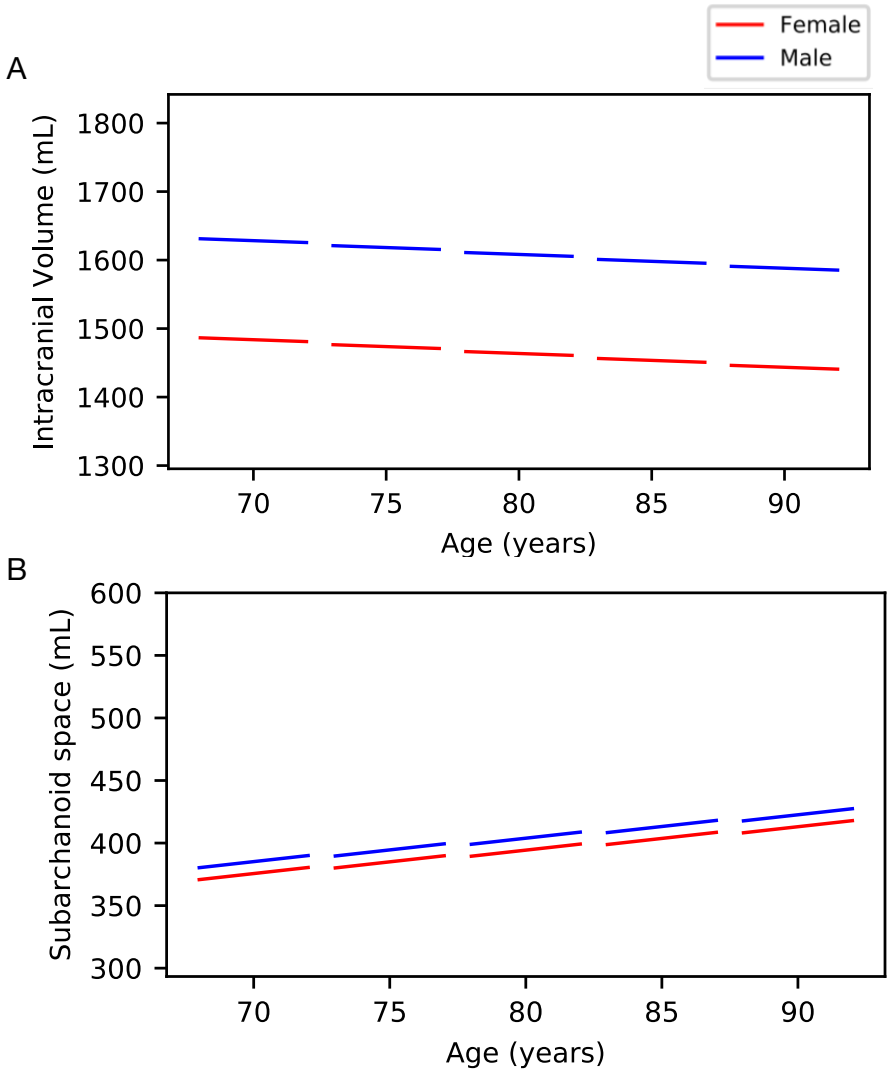

Figure 4-4. The longitudinal trajectories of fixed effects for ICVs and SAS volumes. The trajectories are calculated by applying the fitted coefficients (β in Table 4-I) to the fixed effects. Each solid line segment is is plotted with the baseline age at its start year and with follow-up intervals covering 5 years. Males and females are plotted in blue and red, respectively. (A) is ICVs, and (B) is SAS volumes. In (B), we set the average ICV for both sexes 1526 mL in the fitted LME model to plot the volumes after adjusting for ICV.

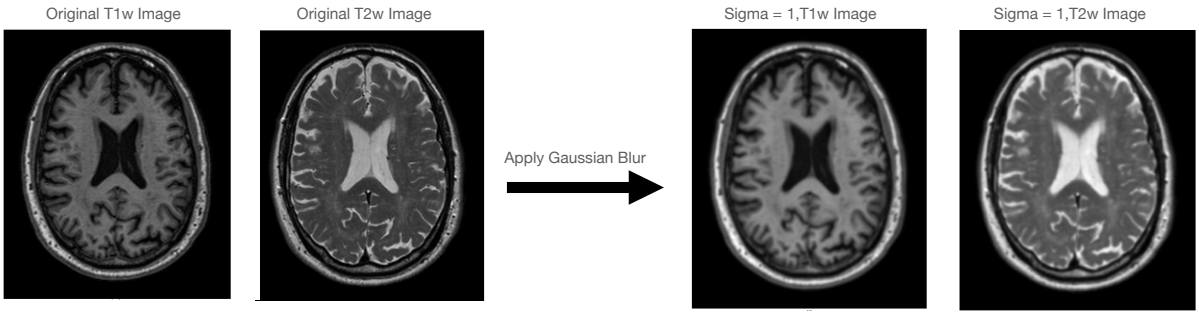

Figure 4-5. Gaussian filters are applied to input paired T1w, T2w images. One example result is is shown with $\sigma = 1$. The left images are paired original inputs and images on the right are resulting images after blurring

the calculation of ICV. We used Gaussian filters to simulate partial volume effects of MR images to ensure the robustness of our trained U-Net CNN. We applied Gaussian filters with 10 different σ values (ranging from 0.1 to 1 to blur paired T1w and T2w images and fed them into our 2D U-Net CNN) to see if the ICV is any different with different σ values (different degrees of partial volume effects). Fig. 4-5 shows an example result of applying Gaussian blur to the input MR images The volume differences were compared between the output masks predicted from Gaussian blurred inputs to the output masks predicted from the original paired T1w and T2w images. The average volume differences across all subjects were calculated for Gaussian blurred output volumes minus the original volume predictions, and the results are shown in Fig. 4-6. One can observe that as the σ value increases, ICV volume differences also increase. We can also observe that partial volume effects cause the overestimation of ICV volumes. The maximum mean change observed at σ value equals 1 was only 12.6 ml, which is small compared to the average total ICV. Thus, we can conclude that even though our algorithm could be affected by partial volume effects, the result of our ICV prediction is not mainly affected by partial volume effects.

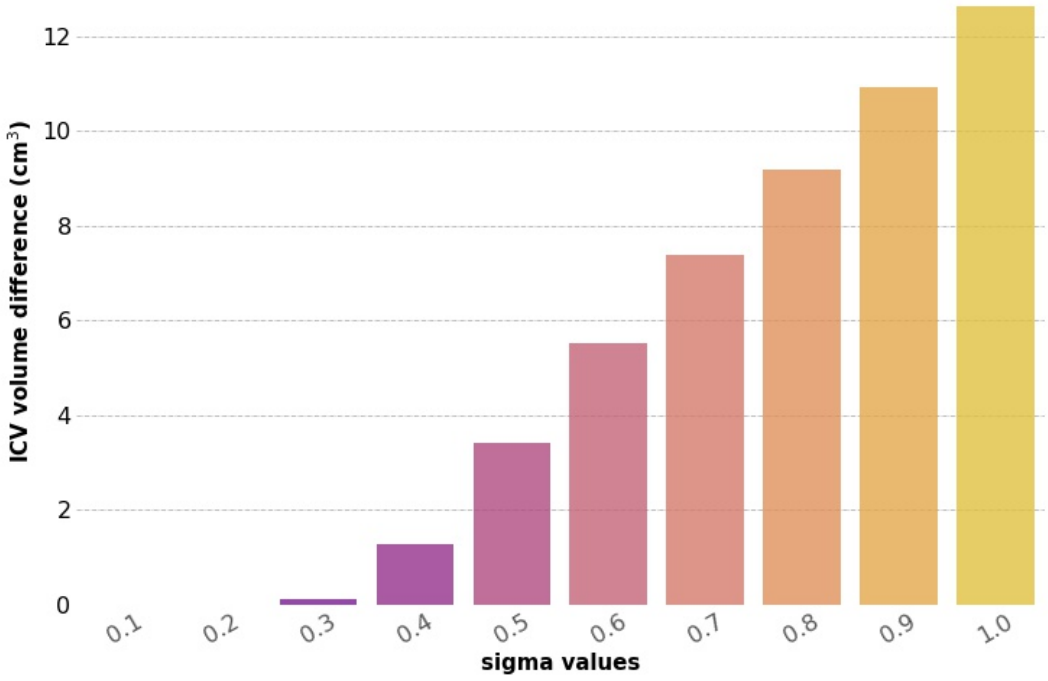

Figure 4-6. The average values for the ICV changes for every subject are calculated for each sigma value of Gaussian blur. The average change of ICV increases as the blur kernel increases its sigma value.

4.4 Label Marching and Dura Thickness Calculation

The fast marching algorithm was used to extend the voxel labels outside the pial surface to the outer surface of the dura (epidural surface) as shown in Fig. 4-7. This extended mapping of the brain regions serves as a reference for meningeal thickness mapping for future calculations. It allows the calculated thickness to be assigned to different brain regions. The labels come directly from an existing algorithm SLANT-CRUISE [43, 44]. The labels from SLANT-CRUISE [43, 44] include regions of the inner brain, which should not be marched out to the meninges. To ensure the accuracy of the meninges labelling, we manually selected labels only associated with the cortical surface of the brain. These labels were then divided into 5 main cortical regions: the frontal lobe, the temporal lobe, the parietal lobe, the occipital

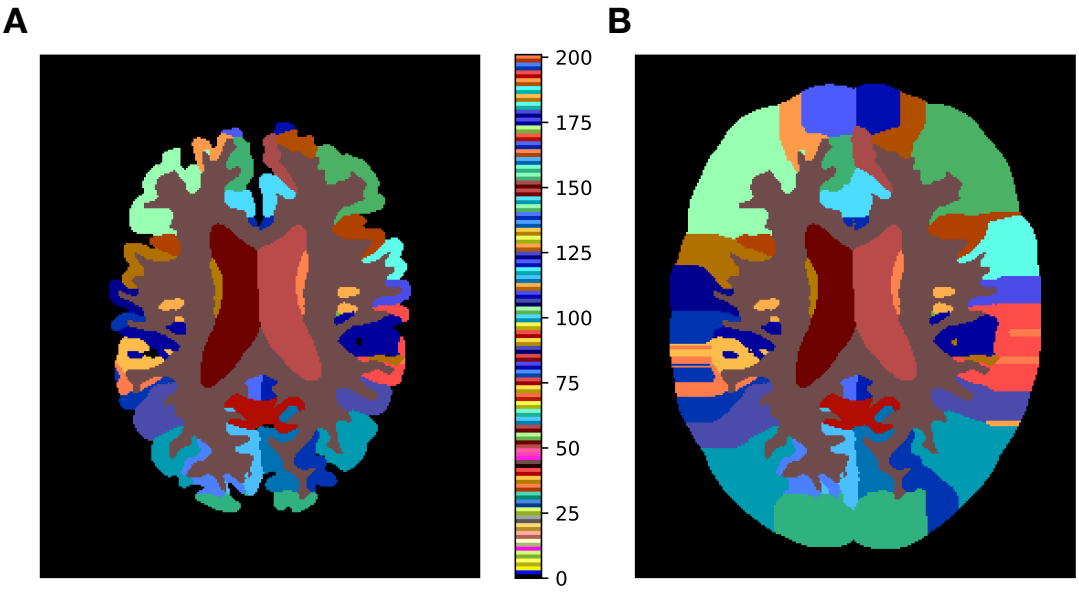

Figure 4-7. Fast marching algorithm was used to extend the brain segmentation labels from SLANT (A) to the outside of the pia surface but terminated when the level sets evolved to the boundary of the brain mask (B)

lobe, and limbic cortex. We then compared our fast marching result labels with the list we manually generated. By comparing the meningeal layer fast marching label results with the cerebral cortex labels list, we were able to confirm the meningeal fast marching labels are marched from cortical regions of the brain.

For meningeal layer thickness calculation, we selected the dura as a starting point for meningeal layer thickness calculations. Our ICV LME analysis results show that ICV decreases with normal aging. Since dura is directly adherent to the skull's inner surface, we are interested in whether dura thickness changes with normal aging. The pilot study was only carried out on one scan of five randomly selected BLSA subjects to find their dura

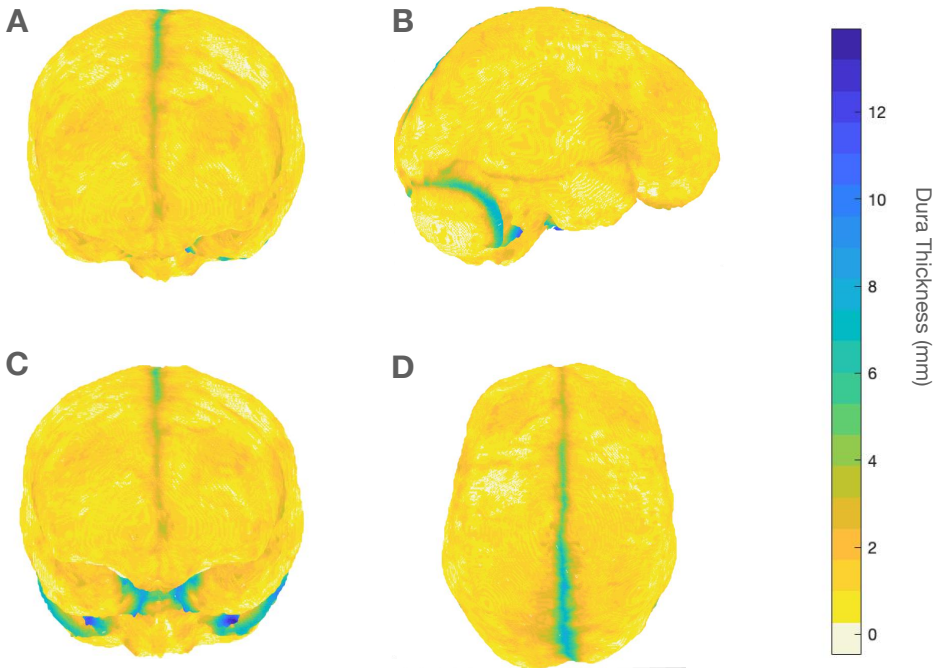

Figure 4-8. An example dura thickness calculation mapped to the dura mesh result is shown in different views. (A),(B),(C), and (D) show the front, side (right), back, and top view of the brain respectively. The color bar on the right side shows the thickness values in units of millimeters. The thicker regions are shown as white and light yellow colors, the thinner regions are shown as black or red colors.

thickness. For visualization of the results on the mesh, the thickness result were mapped back to the mesh space by assigning each vertex the same signed distance as calculated from the rounded coordinates. Therefore, vertices with the same rounding result may have the same thickness. Figure 4-8 shows results visualized with 3D surface mesh. From an initial investigation, we see that dural sinuses have greater thicknesses than other regions of the dura. Our preliminary results can be applied to more subjects in the future to find longitudinal and regional changes.

Chapter 5

Discussion and Conclusions

We described a method to reconstruct the meningeal surfaces using CNNs and NTGDMs. The NTGDMs were performed as a post-processing step of the CNNs in our work. Our algorithm was applied to subjects from the BLSA to study longitudinal changes in ICVs and SAS volumes. We found that the coefficients of the baseline age and follow-up the interval for the SAS volume was significantly different from 0, suggesting that the SAS volume is larger at a higher age and increases over time. It is surprising that the ICV decreases longitudinally based on our result even though ICVs are generally assumed to be constant after peaking in early adulthood [53]. We validated our algorithm to reassure the ICV measurement were not from algorithm bias. We argue that the decrease we observed in ICV analysis could be due to our limited sample size but we also note that a previous study using T1w brain scans found a ICV decrease starting from the middle adulthood [26].

To further investigate in the ICV decrease, we conducted a pilot study with only five randomly selected BLSA subjects to find their dura thickness changes during aging. We used fast marching to march the cortical brain labels into the meninges so that we can region match the thickness changes in the future. We can calculate thickness on more subjects and investigate the longitudinal thickness changes during normal aging.

Although for the SAS analysis, we have only reported volumes of SAS, it is also feasible to analyze the thicknesses of the SAS using regional label mappings, both globally and locally,

from our surface reconstructions. In the future, we also plan to apply our algorithm to other cohorts to help us better understand brain atrophy during aging and could extend our cohorts to diseased individuals. We are also investigating more advanced algorithms to incorporate the topology constraint and the anatomical ordering of the meninges into CNNs for future studies.

Based on the longitudinal statistical analysis results, We first validated our algorithm based on the linear mixed model results of SAS and ICV by applying Gaussian filters to the network input. After the validation step, we conducted a preliminary study on 5 subjects from BLSA and analyzed their longitudinal change of dura thickness in different brain regions. The region mapping was done using an existing algorithm called fast marching [16] and dura thickness is calculated by the signed distance between the 2 layers of the meninges. In the future, we are planning on running the algorithm on a larger dataset to analyze the ICV and SAS longitudinal change in the not only aging group but maybe also in the diseased group. We also want to further investigate the changes observed in ICV and SAS and conduct more accurate region mapping to calculate the regional thickness of different meningeal structures.

References

1. Nguyen, B. & et al. Basal lamina changes in neurodegenerative disorders. *Molecular Neurodegeneration* **16,** 81 (2021).

2. Montagne, A. & et al. Brain imaging of neurovascular dysfunction in alzheimer's disease. *Acta Neuropathologica* **131,** 687–707 (2016).

3. Kisler, K. & et al. Cerebral blood flow regulation and neurovascular dysfunction in alzheimer disease. *Nature Reviews Neuroscience* **18,** 419–434 (2017).

4. Turtzo, L. C. & et al. Meningeal blood–brain barrier disruption in acute traumatic brain injury. *Brain Communications* **2** (2020).

5. Walsh, D. R. & et al. Mechanical properties of the cranial meninges: A systematic review. *Journal of Neurotrauma* **38,** 1748–1761 (2021).

6. Scahill, R. I. & et al. Mapping the evolution of regional atrophy in Alzheimer's disease: unbiased analysis of fluid-registered serial MRI. *Proceedings of the National Academy of Sciences* **99,** 4703–4707 (2002).

7. Fan, Y. & et al. Spatial patterns of brain atrophy in MCI patients, identified via high-dimensional pattern classification, predict subsequent cognitive decline. *NeuroImage* **39,** 1731–1743 (2008).

8. Jones, O. *The Meninges* https://teachmeanatomy.info/neuroanatomy/structures/meninges/ (2022).

9. Voevodskaya, O. & et al. The effects of intracranial volume adjustment approaches on multiple regional MRI volumes in healthy aging and Alzheimer's disease. *Frontiers in Aging Neuroscience* **6,** 264 (2014).

10. Han, S. & et al. Longitudinal analysis of regional cerebellum volumes during normal aging. *NeuroImage* **220,** 117062 (2020).

11. Pham, D. L. & et al. Current Methods in Medical Image Segmentation. *Annual Review of Biomedical Engineering* **2,** 315–337 (2000).

12. Yushkevich, P. A. & et al. User-Guided 3D Active Contour Segmentation of Anatomical Structures: Significantly Improved Efficiency and Reliability. *NeuroImage* **31,** 1116–1128 (2006).

13. Glaister, J. & et al. *Deformable model reconstruction of the subarachnoid space* in *Medical Imaging 2018: Image Processing* **10574** (2018), 793–799.

14. Han, X. & et al. CRUISE: Cortical reconstruction using implicit surface evolution. *NeuroImage* **23,** 997–1012 (2004).

15. Shock, N. W. & et al. Normal human aging: the Baltimore longitudinal study of aging. *Washington, DC. US Government Printing Office.* (1984).

16. Sifakis, E. & Tziritas, G. in. Chap. Geometric Level Set Methods in Imaging, Vision and Graphics (Springer, 2003).

17. Fam, M. & et al. Skull base dural thickness and relationship to demographic features: A postmortem study and literature review. *Journal of Neurological Surgery Part B: Skull Base* **79,** 614–620 (2018).

18. Reina, M. A. & et al. structure of the arachnoid layer of the human spinal meninges: A barrier that regulates dural sac permeability. *Revista espanola de anestesiologia y reanimacion* **57,** 486–492 (2010).

19. Shafique, S. & Rayi, A. *Anatomy, head and neck, Subarachnoid Space* 2021.

20. Veening, J. G. & Barendregt, H. P. The regulation of brain states by neuroactive substances distributed via the cerebrospinal fluid; a review. *Cerebrospinal Fluid Research* **7** (2010).

21. Betts, J. G. & et al. *Anatomy and Physiology* (2013).

22. Bazin, P.-L. & et al. A computational framework for ultra-high resolution cortical segmentation at 7Tesla. *NeuroImage* **93.** In-vivo Brodmann Mapping of the Human Brain, 201–209 (2014).

23. Viviani, R. & et al. Multimodal MEMPRAGE, FLAIR, and R2* Segmentation to Resolve Dura and Vessels from Cortical Gray Matter. *Frontiers in Neuroscience* **11** (2017).

24. Liu, R. & et al. A longitudinal study of brain morphometrics using quantitative magnetic resonance imaging and difference image analysis. *NeuroImage* **20,** 22–33 (2003).

25. Royle, N. & et al. Influence of thickening of the inner skull table on intracranial volume measurement in older people. *Magnetic Resonance Imaging* **31,** 918–922 (2013).

26. Caspi, Y. & et al. Changes in the intracranial volume from early adulthood to the sixth decade of life: A longitudinal study. *NeuroImage* **220,** 116842 (2020).

27. Gopinath, K. & et al. *SegRecon: Learning Joint Brain Surface Reconstruction and Segmentation from Images* in *Medical Image Computing and Computer Assisted Intervention – MICCAI 2021* (2021), 650–659.

28. Henschel, L. & et al. FastSurfer - A fast and accurate deep learning based neuroimaging pipeline. *NeuroImage* **219,** 117012 (2020).

29. Wickramasinghe, U. & et al. *Voxel2Mesh: 3D Mesh Model Generation from Volumetric Data* in *Medical Image Computing and Computer Assisted Intervention – MICCAI 2020* (2020), 299–308.

30. Ma, Q. & et al. *PialNN: A Fast Deep Learning Framework for Cortical Pial Surface Reconstruction* in *International Workshop on Machine Learning in Clinical Neuroimaging* (2021).

31. Bongratz, F. & et al. Vox2Cortex: Fast Explicit Reconstruction of Cortical Surfaces from 3D MRI Scans with Geometric Deep Neural Networks. arXiv:2203.09446 (2022).

32. Cruz, R. & et al. *DeepCSR: A 3D Deep Learning Approach for Cortical Surface Reconstruction* in *2021 IEEE Winter Conference on Applications of Computer Vision (WACV)* (2021), 806–815.

33. Leslin, C. M. & et al. TOPOFIT-DB, a database of protein structural alignments based on the TOPOFIT method. *Nucleic Acids Research* **35,** D317–D321 (2006).

34. Tustison, N. J. & et al. N4ITK: improved N3 bias correction. *IEEE Transactions on Medical Imaging* **29,** 1310–1320 (2010).

35. Reinhold, J. C. & et al. *Evaluating the impact of intensity normalization on MR image synthesis* in *Medical Imaging 2019: Image Processing* **10949** (2019), 109493H.

36. Zhao, C. & et al. SMORE: A Self-Supervised Anti-Aliasing and Super-Resolution Algorithm for MRI Using Deep Learning. *IEEE Transactions on Medical Imaging* **40,** 805–817 (2021).

37. Zhao, C. & et al. Applications of a deep learning method for anti-aliasing and super-resolution in MRI. *Mag. Reson. Im.* **64,** 132–141 (2019).

38. Fonov, V. S. & et al. Unbiased nonlinear average age-appropriate brain templates from birth to adulthood. *NeuroImage* **47,** S102 (2009).

39. Singh, M. & et al. *Accurate estimation of total intracranial volume in MRI using a multi-tasked image-to-image translation network* in *Medical Imaging 2021: Image Processing* **11596.** SPIE (2021), 110–117.

40. Roy, S., Butman, J. A. & Pham, D. L. Robust skull stripping using multiple MR image contrasts insensitive to pathology. *NeuroImage* **146,** 132–147 (2017).

41. Zuo, L. & et al. *Information-based disentangled representation learning for Unsupervised MR Harmonization* in *Information Processing in Medical Imaging* (2021), 346–359.

42. Zuo, L. & et al. Unsupervised MR harmonization by learning disentangled representations using information bottleneck theory. *NeuroImage* **243,** 118569 (2021).

43. Huo, Y. & et al. 3D whole brain segmentation using spatially localized atlas network tiles. *NeuroImage* **194,** 105–119 (2019).

44. Huo, Y. *et al.* Consistent cortical reconstruction and multi-atlas brain segmentation. *NeuroImage* **138,** 197–210 (2016).

45. Ronneberger, O. & et al. *U-Net: convolutional networks for biomedical image segmentation* in *Medical Image Computing and Computer-Assisted Intervention (MICCAI)* (2015), 234–241.

46. Mescheder, L. & et al. *Occupancy Networks: Learning 3D Reconstruction in Function Space* in *2019 IEEE/CVF Conference on Computer Vision and Pattern Recognition (CVPR)* (2019), 4455–4465.

47. Kingma, D. P. & Ba, J. *Adam: a method for stochastic optimization* arXiv:1412.6980. 2014.

48. Roy, S. & et al. Robust skull stripping using multiple MR image contrasts insensitive to pathology. *NeuroImage* **146,** 132–147 (2017).

49. Bazin, P.-L. & Pham, D. L. Topology correction of segmented medical images using a fast marching algorithm. *Computer Methods and Programs in Biomedicine* **88,** 182–190 (2007).

50. Pinheiro, J. C. & Bates, D. M. Linear mixed-effects models: basic concepts and examples. *Mixed-effects models in S and S-Plus,* 3–56 (2000).

51. Brown, V. A. An introduction to linear mixed-effects modeling in R. *Advances in Methods and Practices in Psychological Science* **4** (2021).

52. Pinheiro, J. & et al. *`nlme`: Linear and Nonlinear Mixed Effects Models* R package version 3.1-140 (2019).

53. Royle, N. A. & et al. Influence of thickening of the inner skull table on intracranial volume measurement in older people. *Magn Reson Imaging* **31,** 918–922 (2013).

Peiyu Duan

pduan2@jh.edu

Education

Johns Hopkins University **Sep. 2020 – May 2022**
M.S.E. in Biomedical Engineering *Baltimore, MD*

University of Wisconsin-Madison **Sep. 2016 – May 2020**
B.S. in Biomedical Engineering *Madison, WI*

- Awards and Honors:Dean's List for 2016 and 2017 Fall; Dean's Honor List for 2018 Fall, 2019 Spring and 2020 Spring; Martha Helen & Walker George Dollmeyer BME Scholarship Award

Publication

- **P. Duan**, S. Han, L. Zuo, Y. An, Y. Liu, A. Carass, S.M. Resnick, and J.L. Prince, "Cranial meninges reconstruction based on convolutional networks and deformable models: Applications to longitudinal study of normal aging", SPIE Conference on Medical Imaging 2022, accepted oral presentation Oct. 2021
- L. Zhang, Y. Du, J. Li, **P. Duan**, X. Zhang; L. Huang, C. Qiao,"Risk factor of intrauterine haematoma among recurrent pregnancy loss patients: a retrospective cohort study in Northeast China",European Journal of Obstetrics & Gynecology and Reproductive Biology, submitted July 2022

Research Experience

The Image Analysis and Communications Lab **Nov. 2020 – now**
Research Assistant with Prof. Jerry L. Prince *Baltimore, MD*

- Assisted in developing an automated algorithm to reconstruct the cranial meninges and segment the subarachnoid space and dural sinuses from conventional T1w and T2w MRI
- Conducted longitudinal statistical analysis of the intracranial volume (ICV) and subarachnoid space (SAS) volume through linear mixed model
- Worked on manual delineation for labeling the brain meninges using ITKSnap

Maternal and Fetal Medicine Lab **Apr.2020 – Nov. 2020**
Research Assistant with Prof. Chong Qiao *Shenyang, China*

- Assisted in data cleaning using R and statistical analysis for risk factors of intrauterine hematoma (IUH) in recurrent pregnancy loss (RPL) and non-RPL patients using SPSS and Python
- Conducted literature review and found specific region of interest on ultrasound image for intrauterine hematoma. Tried to adopt machine learning algorithms for ultrasound image segmentation
- Edited manuscript as fourth author for European journal of obstetrics & gynecology and reproductive biology

Laryngeal Physiology Laboratory **Feb. 2019 – Mar. 2020**
Undergraduate Research Assistant with Dr. Jack Jiang *Madison, WI*

- Assisted in applying Clarity technique to compare collagen level between pathological and healthy vocal fold tissue
- First author on manuscript of a calibration curve between frequency and permitivity for the vocal fold
- Conducted in-depth research on children with vocal disorders to compare vocal offset and onset vocal frequency with adults
- Worked with Taiwan larynges device company and performed data analysis on larynges implant testing

The Tibbetts Lab **Nov. 2017 – Dec. 2018**
Undergraduate Research Assistant with Prof. Randal Tibbetts *Madison, WI*

- Conducted research on Activating Transcription Factor (ATF1) for understanding cAMP response element-binding protein (CREB) signaling in cell growth, metabolism, synaptic plasticity
- Gained profound laboratory skills through performing mini & midi prep, DNA sequencing, bacteria transformation, PCR, western blotting, and tissue engineering techniques

Teaching Experience

Cell and Tissue Engineering Teaching Assistant **Aug. 2021-Now**
Johns Hopkins University *Baltimore, MD*

- Answer student emails and discussion questions
- Grade student homework on a weekly basis
- Hold occasional office hour for students

Biomedical Engineering Practice and Innovation Teaching Assistant Jun. 2021 – Aug. 2021
Johns Hopkins University *Baltimore, MD*

- Host office hour to answer homework questions and teach MATLAB software
- Assisted professors to grade and create answer keys for homework

Academic Projects

Arm Support System for SMA kid | *Team Leader* **Spring 2020**

- Designed an arm support system for a 4-year-old girl with the help from occupational therapist Megan Shiele
- The design helped lift both arms and wrists for her to practice grabbing and playing with toys

Skull Entry Device | *Team Leader* **Fall 2019**

- Fabricated a skull entry locating device for neurosurgeon Dr. Azam Ahmed with 3D printed arch and cam lock system
- The device can be personally applied to each patient based on their MRI scan of the head and 3D printing the head
- In comparison of current locating procedure that takes 30 minutes, the new device takes only 5 minutes within error distance of 3.44 mm, which would significantly save time for surgeon and save money for patient

Easier Access to Cerebrospinal Fluid Using Augmented Reality | *Team Leader* **Fall 2018**

- Developed a holographic application with the Microsoft product, Hololens, and 3D CT scans of the patient's lumbar spine
- CT scan of individual patients can be loaded into Hololens to aid physician perform lumbar puncture for overweight patients
- Statistical analysis by way of a paired t-test indicated the success rate of group members wearing the goggles was significantly higher than without goggles at the 95% confidence level

Language and Skills

Technical competencies: Python, R, MATLAB, VS Code, Latex, SolidWorks, Linux, GitHub , Microsoft Suites

Languages: English (proficient), Mandarin Chinese (native speaker), Spanish (communication-based)

Volunteer Experience

Oncology Pharmacy **Jan. 2018-Dec.2018**
UW Health University Hospital *Madison, WI*

- Organize medicine shelves and check medicine expiration dates and put labels on medicine bottle accordingly
- Print out back labels for pharmacists and match patient names

Infection Control **Sep. 2017-Dec.2017**
UW Health University Hospital *Madison, WI*

- Observe and record doctors and nurses entering room with infection disease patients if they put on proper clothes and followed cleaning protocols before entering the room
- Examine infection control room patients and family members following protocols and examine whether infection control rooms have sufficient supplies